

Host-star and exoplanet composition: Polluted white dwarf reveals depletion of moderately refractory elements in planetary material^{*}

Claudia Aguilera-Gómez^{1,2}, Laura K. Rogers³, Amy Bonsor³, Paula Jofré^{4,2}, Simon Blouin⁵, Oliver Shorttle³, Andrew M. Buchan⁶, Yuqi Li³, and Siyi Xu⁷

¹ Instituto de Astrofísica, Pontificia Universidad Católica de Chile, Av. Vicuña Mackenna 4860, 782-0436 Macul, Santiago, Chile
e-mail: craguile@uc.cl

² Millennium Nucleus ERI

³ Institute of Astronomy, University of Cambridge, Madingley Road, Cambridge CB3 0HA, UK

⁴ Instituto de Estudios Astrofísicos, Universidad Diego Portales, Av. Ejército Libertador 441, Santiago, Chile

⁵ Department of Physics and Astronomy, University of Victoria, Victoria, BC V8W 2Y2, Canada

⁶ Department of Physics, University of Warwick, Coventry CV4 7AL, UK

⁷ Gemini Observatory/NSF's NOIRLab, 670 N. A'ohoku Place, Hilo, HI 96720, USA

Received X, 2024; accepted X, 2024

ABSTRACT

Context. Planets form from the same cloud of molecular gas and dust as their host stars. Confirming if planetary bodies acquire the same refractory element composition as their natal disc during formation, and how efficiently volatile elements are incorporated into growing planets, is key to linking the poorly constrained interior composition of rocky exoplanets to the observationally-constrained composition of their host star. Such comparisons also afford insight into the planet formation process.

Aims. This work compares planetary composition with host-star composition using observations of a white dwarf that has accreted planetary material and its F-type star wide binary companion as a reference for the composition of the natal molecular gas and dust.

Methods. Spectroscopic analysis reveals abundances of Fe, Mg, Si, Ca, and Ti in both stars. We use the white dwarf measurements to estimate the composition of the exoplanetary material and the F-type companion to constrain the composition of the material the planet formed from.

Results. Comparing planetary material to the composition of its natal cloud, our results reveal that the planetary material is depleted in moderate refractories (Mg, Si, Fe) relative to the refractory material (Ca, Ti). Grouping elements based on their condensation temperatures is key to linking stellar and planetary compositions.

Conclusions. Fractionation during formation or subsequent planetary evolution leads to the depletion of moderate refractories from the planetary material accreted by the white dwarf. This signature, as seen for bulk Earth, will likely be present in the composition of many exoplanets relative to their host-stars.

Key words. Stars: abundances – Stars: binaries: general – Stars: white dwarfs – Planets and satellites: composition – Planets and satellites: formation

1. Introduction

The intricate process of planet formation remains one of the most challenging frontiers of modern astrophysics. Stars and planets form from the collapse of a cloud of interstellar gas and dust (Wang et al. 2019; Adibekyan et al. 2021). As planets form, volatile elements, characterized by low condensation temperatures, are not present in solid form at high temperatures close to the host star. In contrast, the most refractory elements remain in solid form and likely present in growing planets in roughly the same relative proportions as in the star. Moderately volatile and refractory elements fall between these extremes, and their presence in growing planets will be sensitive to the temperature of their formation environment. Additionally, subsequent processing of the planet during the post-nebular phase could further drive the loss of moderately volatile and moderately refractory elements due to impacts and melting. These processes imply that

the composition of an exoplanet, unknown in detail, cannot be simply linked to that of its host star. Exoplanet detection techniques yield a planet's mass and radius and can only provide information on the bulk density, leaving degeneracies in determining its true composition (e.g. Seager et al. 2007; Dorn et al. 2015). As the composition of a planet is paramount for unraveling its interior structure, there is a challenge in using stellar compositions to constrain planet structure. Better insights into how stellar compositions, or the composition of the primordial material, map to planetary compositions would alleviate this.

As host stars and their planets form from the same cloud of interstellar gas, the host stars are invaluable objects for understanding the composition of exoplanets. In particular, the chemical composition of a star provides crucial insights into the primordial material available to form the exoplanets (Thiabaud et al. 2015). A valuable approach, then, is comparing the host star's composition with that of the bulk planet composition in the context of our Solar System. Here, the analysis of meteorites provides a window into the study of rocky planetary material.

^{*} This paper includes data gathered with the 6.5 meter Magellan Telescopes located at Las Campanas Observatory, Chile.

The abundance of refractory elements, such as Ca, Al, and Ti, in chondritic meteorites, agrees with the composition of the Sun (Anders & Ebihara 1982), although with slight variations in elemental ratios, underscoring the complexity of the planet formation process. In contrast, there is a depletion of volatile elements. Wang et al. (2018) documents that moderately refractory elements like Si, Mg, Fe, and Ni exhibit subtle differences between the Sun and the Earth, while elements such as C and S experience substantial depletion.

White dwarfs (WDs) present an additional avenue for acquiring the bulk composition of planetesimals. These stellar remnants do not retain the chemical characteristics of their progenitors and typically exhibit pure hydrogen or helium atmospheres (e.g. Koester et al. 2009). Heavier elements, on the other hand, are expected to sink out from the visible layers in timescales much shorter than the cooling age of the WD. As such, the presence of metals in the spectra of WDs serves as an indication of accretion from smaller rocky bodies that have endured the host star's evolution and subsequently been scattered inwards, undergoing tidal disruption by the WD (Veras 2016). Approximately 20–50% of WDs display signs of pollution (e.g. Koester et al. 2014), with compelling evidence suggesting the ingestion of planetary material to account for this phenomenon (Jura 2003). This hypothesis is further supported by the evidence for circumstellar discs of gas and dust (e.g. Gänsicke et al. 2006; Farhi 2016), transits of disrupted bodies (Vanderburg et al. 2015; Guidry et al. 2021), and X-ray signals indicative of ongoing accretion (Cunningham et al. 2022).

These metal polluted WDs have served as valuable tools for studying the composition of accreted planetesimals and delving into the geology of exoplanetary material (e.g. Harrison et al. 2018; Swan et al. 2023). The abundance of specific elements detected in the WD atmosphere offers crucial insights into the process of planet formation itself and of the subsequent heating of the planetesimal. Analyzing the amount of volatiles provides estimations of the planets' formation radius in the disc, the ratio of different types of elements aids in understanding the formation of planetary cores and crusts, and the accretion of icy objects provides insights into the cores of giant planets (e.g. Harrison et al. 2018; Gänsicke et al. 2019; Harrison et al. 2021a).

Host star compositions are often used as a proxy for exoplanetary compositions. While a similar agreement in refractory composition between the host star and exoplanet and a considerable depletion of volatiles in the planetesimals might be expected, it remains unconfirmed and rigorous testing is essential. The bulk composition of exoplanetary material, a puzzle WDs help solve, offers a crucial piece of this testing process. However, WDs alone cannot provide the host star's composition. To address this, binary star systems present a unique opportunity. Just as planets and stars, binary systems form out of the collapse of the same cloud of interstellar gas and have similar ages and initial compositions, especially if the components of the system evolve independently, as is the case for wide binaries. Such stars have been found to be more chemically homogeneous than random stars in the field (Andrews et al. 2019; Hawkins et al. 2020; Espinoza-Rojas et al. 2021). Although other theories for the formation of these systems have been suggested, the components of wide binaries are still expected to have similar ages and elemental abundances.

Examining wide binary systems with a metal polluted white dwarf and a main sequence (MS) companion unveils a promising avenue to utilize the shared origins of stellar siblings and their planets in deciphering the mysteries of exoplanet formation. The initial conditions of the system are determined by ana-

lyzing the spectra of the wide binary companion, still on the MS, and the composition of the exoplanetary material can be inferred from the spectrum of the metal polluted WD. In Bonsor et al. (2021), a pilot study is presented, using optical high-resolution spectra for the K-dwarf G200-40, a wide binary companion to the metal polluted white dwarf WD 1425+540. Abundances of C, N, O, Mg, Si, S, Ca, Fe, and Ni for the white dwarf suggested the ingestion of a rocky body rich in volatile elements (Xu et al. 2017). Bonsor et al. (2021) measured the chemical abundances of the K-companion and found that the refractory composition of the companion matched with the bulk exoplanetary material within the observational errors. However, C/Fe appeared to be depleted in the white dwarf planetary material compared to its host star. This is consistent with volatile depletion in planetesimals. Throughout this work, we use different notations for abundances. The notation X_1/X_2 refers to the logarithmic number abundances of element X_1 relative to element X_2 . In contrast, the notation $[X_1/X_2]$ represents abundances with respect to solar values, defined as $[X_1/X_2] = \log(X_1/X_2) - \log(X_1/X_2)_\odot$, where $\log(X_1/X_2)_\odot$ is the solar abundance ratio.

Each new system under examination offers a unique window into planet formation and the geological processing of planetary material (e.g., volatile depletion), depending on the elements found in the white dwarf spectrum. In this study, we present a comprehensive chemical analysis of the polluted white dwarf SDSS J082019.49+253035.3 (WD J0820 hereafter) and its binary companion HD69962, which is on the main sequence. This binary system, initially identified as a wide binary with main-sequence and white dwarf components by El-Badry & Rix (2018), has been further confirmed by the updated catalog of El-Badry et al. (2021), specifying a projected separation of approximately ~ 7980 au.

Section 2 outlines our schematic representation of the evolution of the system, along with observations for both components, and spectroscopic analysis. In particular, subsection 2.3 presents the stellar parameters and abundances of the MS star while subsection 2.4 presents the abundances derived from the white dwarf spectra. Section 3 shows the determination of the accreted planetary material composition and the comparison between the abundances of the star and the planetesimal, assuming the starting composition of the system is given by the binary companion. Section 4 explores various scenarios to interpret the abundances observed in the white dwarf, accounting for sinking effects, and we summarize our conclusions in Section 5.

2. Concepts, data and methods

2.1. Stellar and planetary evolution

A schematic representation of our binary system's evolution is illustrated in Figure 1. The beginning of this system lies in the two components of the wide binary, originating from the same primordial material and sharing an identical initial composition (A), which also serves as the building blocks for the planetesimals in this system. Throughout the planet formation process, various mechanisms can act to modify the abundance of rocky material within the system (e.g., B). In this work, we will use the term 'element fractionation,' referring to the concentration of elements in the solid phase compared to the gas phase. This term encompasses both incomplete condensation during the cooling of the protoplanetary disc and heating of material in the post-nebular phase. As the host star evolves into a white dwarf, it accretes a fraction of this rocky material that survived stellar evolution (C and D). However, as discussed later (Section 3), the

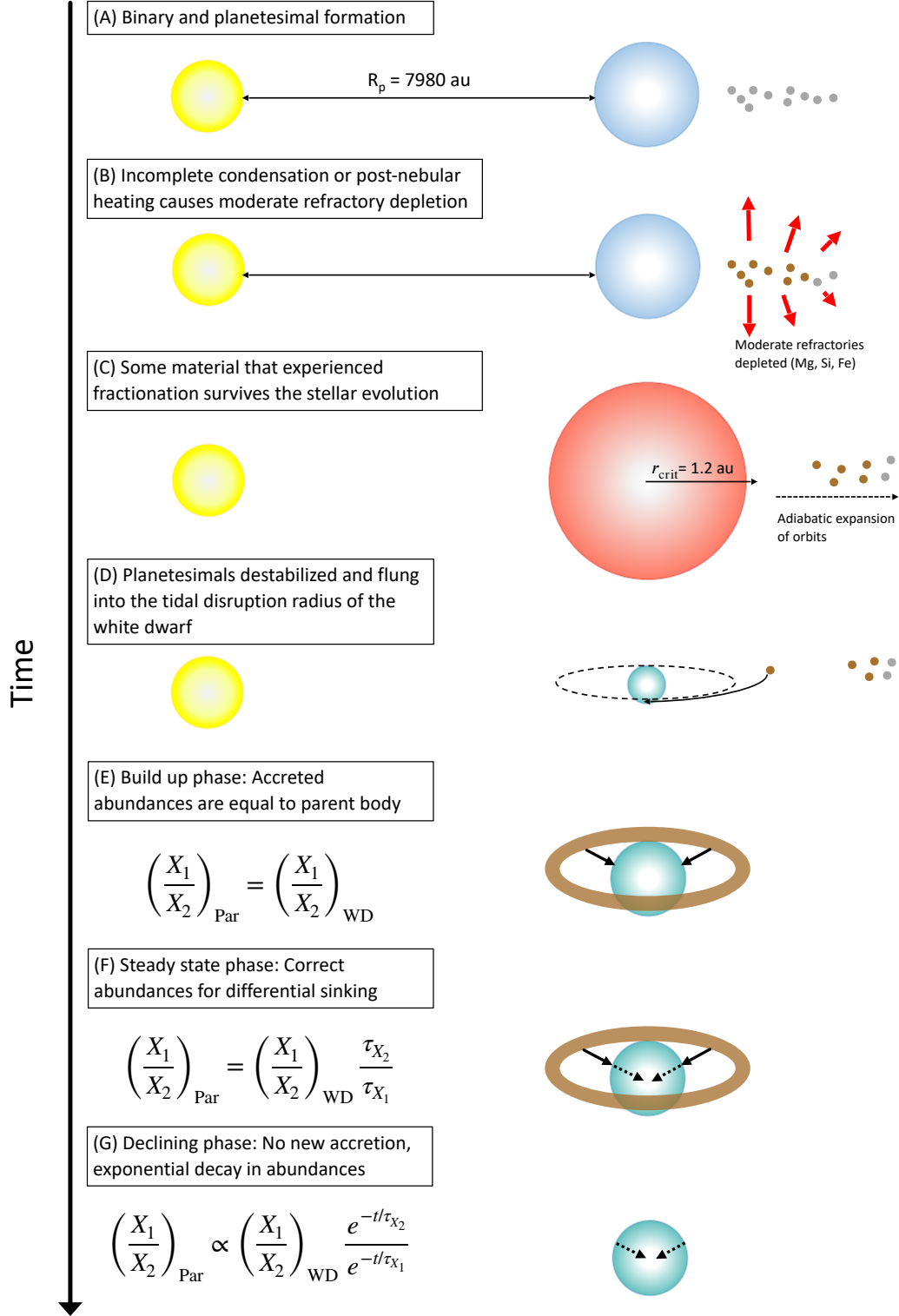


Fig. 1: Formation of the binary and hypothesised evolution of the binary components and planetary material. R_p is the projected separation between the binary components, and r_{crit} is the critical initial semi major axis that a planetesimal must have in order to survive through the stellar evolution to the white dwarf phase assuming an eccentricity of 0. The depletion of moderate refractory relative to refractory elements in (B), indicated by red arrows, can occur both during and after nebula condensation. The different colors of the planetesimals represent whether they have experienced depletion of mildly refractory elements (brown) or not (gray). The white dwarf is being observed in declining phase (G). Equations in phases (E) to (G) show how the relative abundances of elements X_1 and X_2 change from the parent body depending on the accretion phase.

photospheric abundance of the resulting white dwarf may not precisely mirror the composition of the accreted planetary material (E-G).

2.2. Observations

2.2.1. The main sequence star HD69962

We obtained high-resolution, high signal-to-noise (SNR \sim 70) spectra for HD69962 with the Magellan Inamori Kyocera Echelle (MIKE; Bernstein et al. 2003) spectrograph on the 6.5m Magellan Clay Telescope, located at Las Campanas Observatory, over a run in November 2021. MIKE delivers full wavelength coverage from \sim 3500 – 5000 Å in the blue arm and \sim 4500 – 9000 Å in the red. The spectra were obtained with the $0.5'' \times 5.00''$ slit and 1×1 binning, which gives a typical spectral resolution $R=\lambda/\Delta\lambda$ of \sim 55,000 and \sim 45,000 in the blue and red sides respectively. The data were then reduced using the CarPy MIKE pipeline (Kelson et al. 2000; Kelson 2003). We then merge the different echelle orders, normalize the final spectrum using high-order spline fits, and correct to rest-frame using a cross-correlation function with an F-star template. We note that HD69962 also was observed and analyzed as part of the 16th data release of APOGEE (Jönsson et al. 2020). This is an instrument that covers the infrared region, from 1.51 to 1.70 μ m, and has a resolving power of approx. 20,000. We do not analyze this spectrum here but we consider the values reported for comparison with our analysis.

2.2.2. The white dwarf SDSS J082019.49+253035.3

The Sloan Digital Sky Survey (SDSS) observed SDSS J082019.49+253035.3 on 23rd November 2011. The SDSS DR10 spectrum was reported in Kepler et al. (2015); Gentile Fusillo et al. (2015) where it was identified as a DBAZ white dwarf, that is, a white dwarf with a helium dominated atmosphere, also showing hydrogen and heavy elements in its spectra. SDSS has a resolution $R \sim 1800$ and covers the wavelength region from 3550 to 10300 Å with a SNR of 40 around the calcium H and K lines (3934 and 3968 Å).

2.3. Spectroscopic analysis of HD69962

The spectral analysis of the main sequence star HD69962 was done using iSpec (Blanco-Cuaresma et al. 2014; Blanco-Cuaresma 2019). This framework is a python wrapper which includes several radiative-transfer codes, atmospheric models and line lists to measure stellar parameters and abundances with either the synthetic spectral fitting on-the-fly technique or the equivalent width method. In this work, we used spectral synthesis where the code minimizes χ^2 between a synthetic spectrum and observations. To do that, we adopted the MARCS grid (Gustafsson et al. 2008) with the Solar abundance scale of Grevesse et al. (2007) and the code MOOG (2017 version, Sneden 1973), considering local thermodynamic equilibrium.

Figure 2 presents an example region of the stellar spectrum of HD69962 in blue, showing substantial rotational broadening of the lines (for a more detailed discussion, see Sect 4.2.1). In black, we include a spectrum from the Gaia Benchmark Star sample, version 3 (Soubiran et al. 2024), HIP94755, for comparison. The Gaia Benchmark Stars have stellar parameters that are derived using fundamental methods and serve as reference stars beyond the Sun for spectroscopic studies (see also Jofré

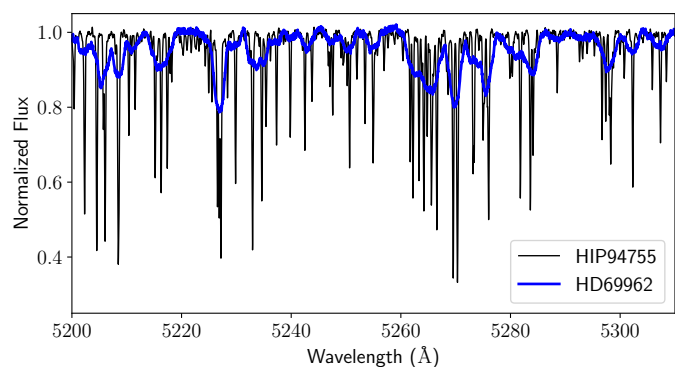


Fig. 2: Region of the HD69962 spectrum compared to the Gaia Benchmark Star HIP94755, with similar atmospheric parameters. HD69962 shows the typical rotational broadening of the lines due to its fast rotation.

et al. 2014; Heiter et al. 2015). HIP94755 has similar parameters to HD69962 (Soubiran et al. 2024), but its rotation is slow. It is due to the rotational broadening that we decided to use the synthesis method with $v \sin i$ as a free parameter to measure the atmospheric parameters and stellar rotation self-consistently. In iSpec, used to fit the spectral lines, resolution, macroturbulence, and projected rotational velocity $v \sin i$ are degenerate parameters, all contributing to the broadening of the lines. As a result, we are unable to fully disentangle these effects. Given that our primary goal was not to obtain precise values for $v \sin i$, but rather to find a consistent line broadening that allowed for the reliable determination of atmospheric parameters and abundances, we did not make additional efforts to separate the individual contributions of these broadening effects. We used the atomic data and line list assembled for the Gaia-ESO Survey (Heiter et al. 2021). Table 1 presents the atmospheric parameters measured for the star. Additionally, we derived a mass estimate of $1.29 \pm 0.20 M_{\odot}$ through the interpolation of MIST (MESA Isochrones and Stellar Tracks) isochrones (Choi et al. 2016). The typical uncertainties associated with these measurements are 150 K for the effective temperature, 0.10 dex for $\log g$, and approximately 7 km/s for $v \sin i$. These substantial uncertainties underscore the challenges encountered during the fitting procedure of synthetic spectra for this star with broadened lines, produced by its rotation.

Given that the spectral synthesis relies on a least-squares method to determine the optimal set of atmospheric parameters producing a synthetic spectrum best matching the observations, the uncertainties for these parameters are calculated from the associated covariance matrix, which in turn depends on the flux errors of our spectrum (Blanco-Cuaresma et al. 2014). To assess the impact of the choice of free variables on our atmospheric results, we re-derived the parameters using different combinations of inputs in iSpec. These included treating microturbulence as a free parameter versus calculating it from empirical relations, and using either both macroturbulence velocity and $v \sin i$ as free parameters or only one as adjustable by the model. In all cases, the differences in the results remained within the range of the reported uncertainties.

Line-by-line abundances were determined using the Gaia-ESO line list as a reference for elemental spectral lines. However, we selectively retained lines based on visual inspection, focusing only on those present in the stellar spectrum. Lines with poor fits, where the synthetic profile deviates significantly

Table 1: Parameters and abundances for HD69962.

-	Optical	APO1	APO2	APO3
T_{eff}	6521	6164	6202	6402
$\log g$	3.86	3.69	3.72	3.81
[Fe/H]	-0.189 ± 0.050	-0.219 ± 0.032	-0.233 ± 0.035	-0.079 ± 0.017
$v \sin i$	63.9	81.3	81.4	82.1
[Mg/Fe]	0.127 ± 0.100	0.241 ± 0.024	0.216 ± 0.025	0.354 ± 0.019
[Si/Fe]	0.132 ± 0.100	0.119 ± 0.027	0.117 ± 0.028	0.163 ± 0.017
[Ti/Fe]	0.193 ± 0.090	-0.483 ± 0.079	0.089 ± 0.084	-
[Ca/Fe]	0.137 ± 0.070	-0.072 ± 0.035	0.132 ± 0.037	-0.179 ± 0.031
[Cr/Fe]	0.188 ± 0.090	0.196 ± 0.059	0.145 ± 0.061	-
[Na/Fe]	0.235 ± 0.08	-1.575 ± 0.063	-0.920 ± 0.064	-
[Ni/Fe]	0.467 ± 0.19	0.020 ± 0.040	0.141 ± 0.043	0.067 ± 0.030

Note: This table includes data from all 3 APOGEE observations and Optical MIKE measurements. Associated uncertainties for chemical abundances are presented alongside each measurement. Notice that the APOGEE observations have some flags reported in the text. The uncertainties for our optical measurements are $u_{T_{\text{eff}}} = 150$ K, $u_{\log g} = 0.10$ dex; $u_{v \sin i} = 7$ km/s. Typical uncertainties reported for APOGEE are $u_{T_{\text{eff}}} \sim 140$ K and $u_{\log g} \sim 0.08$ dex.

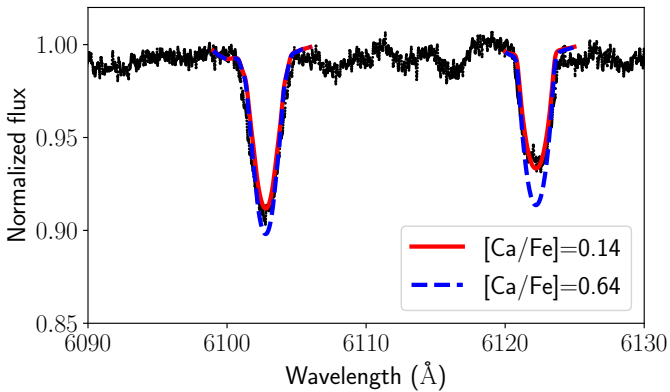


Fig. 3: Sample fit of synthetic Ca lines at 6102.7 and 6122.2 Å (red solid line) to the observed spectrum of HD69962. A synthetic spectrum with 0.5 dex higher Ca is included (blue dashed line) to highlight the difference in abundance between the white dwarf and main sequence star.

from the observed line shape, leading to substantial errors, were filtered out. Subsequently, two iterations of a 2σ -clipping procedure were applied in each chemical abundance. In Table B.1 (Appendix B), we present the final line list for the elements, including the parameters for each line. An illustrative example of Calcium lines, along with their corresponding fit, is depicted in Figure 3. We have included a synthetic spectrum with an abundance 0.5 dex higher than our best fit for the star, similar to the Ca abundance measured for the white dwarf (see Section 2.4), to show that such a high difference would be measurable from the spectrum, confirming the contrast in Ca between main sequence star and white dwarf.

Additionally, this star is included in the APOGEE-2 DR16 (Jönsson et al. 2020) and was analyzed using ASPCAP, the APOGEE Stellar Parameters and Abundances Pipeline. There are three sets of observations for HD69962, with multiple visits each, to which we will refer as APO1, APO2, and APO3 from hereon. All of them have the flag SUSPECT_BROAD_LINES, confirming the broad absorption lines typical of a star with substantial rotation. In Table 1, we include the values reported for all APOGEE observations. These correspond to the calibrated effective temperature, $\log g$ values, reported $v \sin i$, and abun-

dances. A formal discussion on the calibration of parameters can be found in Jönsson et al. (2020). It might be worth mentioning that the uncalibrated values of T_{eff} and $\log g$ are also included in this Data Release and are closer to the values we measure from optical spectra. The APO1 and APO2 observations have the ASPCAP flag COLORTE_WARN, indicating a discrepancy in spectroscopic temperature of more than 500 K with the photometric temperature. Specific parameters can also present flags. For $v \sin i$, all observations have the GRIDEDGE_WARN flag, indicating that the measured rotation rate is close to the edge of the grid.

In addition to the reported flags, Table 1 shows that there can be large discrepancies in the abundances from different APOGEE observations. Although these infrared observations allow us to check the consistency of the measured atmospheric parameters and abundances in general, assessing the accuracy of observations is complicated, and abundances derived from infrared and optical data do not always agree (Jofré et al. 2019; Hegedűs et al. 2023). Moreover, the flags and warnings in the APOGEE analysis and the differences between different observations confirm the difficulty in the derivation of parameters and abundances for this star. Thus, we have decided to include all measurements (3 from APOGEE and our optical determination from MIKE data) in our analysis and discussions.

2.4. Spectroscopic analysis of SDSS J082019.49+253035.3

To determine the white dwarf parameters and abundances of the planetary material accreted by WD J0820, a multi-dimensional grid of 1D model atmospheres with varying effective temperatures, surface gravities, and elemental compositions (Dufour et al. 2007; Blouin et al. 2018) is used to compare with photometric and spectroscopic data. Heavy elements and hydrogen in cooler polluted white dwarfs affect the pressure and temperature structure of the white dwarfs and so affect the derived white dwarf parameters (Dufour et al. 2012; Coutu et al. 2019). Therefore, an iterative procedure was used which alternates between fitting the white dwarf parameters (effective temperature and surface gravity) and the abundances of the metals (Klein et al. 2021). The initial estimates of the white dwarf parameters were determined by using χ^2 minimization to fit the atmospheric models to broad-band SDSS *ugriz* photometry, reported in Table 2, scaling to the distance derived from *Gaia*. Figure 4 shows the spectral energy distribution (SED) of the white dwarf alongside

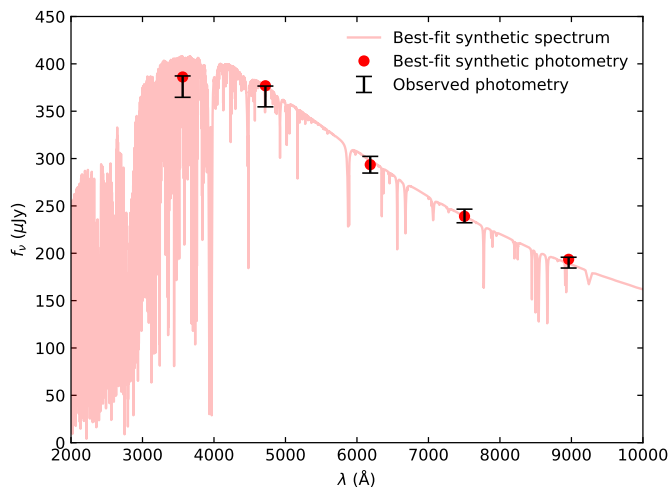


Fig. 4: Spectral energy distribution showing the SDSS *ugriz* photometry for SDSS J082019.49+253035.3 as black error bars, with the best fitting model photometry points as red circles.

with its best-fit spectrum (the same as in Figure A.1). Once a best fitting solution is measured, the white dwarf parameters are fixed whilst the metal abundances are adjusted to fit the absorption lines of the metals in the SDSS spectrum. The photometric fit for the white dwarf parameters and the spectroscopic fit for the metal abundances are repeated until there is internal consistency between them. Fits to specific WD spectral lines can be found in Appendix A.

The final fitted white dwarf parameters and metal abundances are reported in Table 2 and the model fit to the SED is shown in Figure 4. There are two key contributions to the abundance errors of the metals and these were calculated and added in quadrature, the first from the spread in abundances derived from different metal lines of the same element, and the second from the uncertainty in the effective temperature (Klein et al. 2021). The derived white dwarf effective temperature is cooler than those derived in Genest-Beaulieu & Bergeron (2019) (13294 K using a spectroscopic method and 12692 K using a photometric method), however, these differences are naturally explained by the omission of metals in their models. Upper limits of elements not measured in the spectrum were derived by paralleling the methods in Rogers et al. (2024) by finding an equivalent width upper limit that would have led to a 3σ detection for the strongest line for that element in the spectral range of SDSS. Upper limits were found for O, Al, Na, Cr, and Ni and are reported in Table 2.

3. Results

3.1. Primordial material: The abundance of the stellar companion

The chemical abundances of HD69962, detailed in Table 1, are displayed in the abundance ratio plots depicted in Figure 5 alongside with those of Milky Way stars from the field, taken from APOGEE DR16 (Jönsson et al. 2020), and the white dwarf companion. We exclude the measurements of the third APOGEE spectrum (APO3) here due to the absence of Ti abundance, which limit its utility in comparing with planetary composition. APO3 spectral analysis is indeed flagged as "Spectrum has sig-

Table 2: Properties of the white dwarf WD J0820 from *Gaia* DR3 and measured abundances.

Name:	SDSS J082019.49+253035.3	
Gaia source identifier:	679451907694651904	
ICRS RA (deg):	125.0812485217	
ICRS DEC (deg):	25.5097129895	
G (mag)	17.621 (0.001)	
T_{eff} (K):	11900 (320)	
$\log g$ (cm s^{-2}):	8.06 (0.04)	
M_{WD} :	0.619 (0.025)	
$\log q^*$:	-4.99	
u (mag)	17.537 (0.009)	
g (mag)	17.521 (0.005)	
r (mag)	17.754 (0.006)	
i (mag)	17.950 (0.008)	
z (mag)	18.185 (0.024)	
Element X_1	$\log n(X_1)/n(\text{He})$	$[X_1/\text{Fe}]$
H	-5.4 ± 0.10	-3.35
Ca	-6.8 ± 0.10	0.95
Mg	-6.3 ± 0.14	0.24
Fe	-6.6 ± 0.20	0.00
Ti	-8.6 ± 0.20	0.55
Si	-6.2 ± 0.20	0.34
O	< -5.0	< 0.39
Al	< -5.9	< 1.78
Na	< -6.3	< 1.58
Cr	< -6.5	< 1.91
Ni	< -5.7	< 2.12
$\log \tau_{\text{Ca}}$ (yr)	6.18	
$\log \tau_{\text{Mg}}$ (yr)	6.31	
$\log \tau_{\text{Fe}}$ (yr)	6.05	
$\log \tau_{\text{Ti}}$ (yr)	6.09	
$\log \tau_{\text{Si}}$ (yr)	6.28	
$\log \tau_{\text{O}}$ (yr)	6.43	
$\log \tau_{\text{Al}}$ (yr)	6.27	
$\log \tau_{\text{Na}}$ (yr)	6.31	
$\log \tau_{\text{Cr}}$ (yr)	6.07	
$\log \tau_{\text{Ni}}$ (yr)	6.04	

Notes: RA and DEC use epoch 2016. Abundances measured for the white dwarf are presented both in log number abundances relative to He and as abundances relative to solar values. Diffusion timescales from Koester et al. (2014, 2020).

* $q = \log_{10}(M_{\text{CVZ}}/M_{\text{WD}})$, the ratio between the mass of the convective zone of the white dwarf, M_{CVZ} , to the total mass of the white dwarf, M_{WD} .

nificant number ($> 20\%$) of pixels in low persistence region: WARN (PERSIST_LOW)".

When focused on HD69962, we obtain consistent agreements for all abundances between our measurements and APOGEE, except $[\text{Ni}/\text{Fe}]$. For this element, we obtain 0.2 dex higher than APOGEE, and we discuss it further in Sect. 4. Regarding Ti and Ca, our results agree with the measurements reported for APO2 only, and discussions about these measurements can also be found in Sect. 4. Overall, our measurements for the chemical composition of HD69962 align with other stars in the Galaxy, showing this star is a typical star in the solar neighborhood.

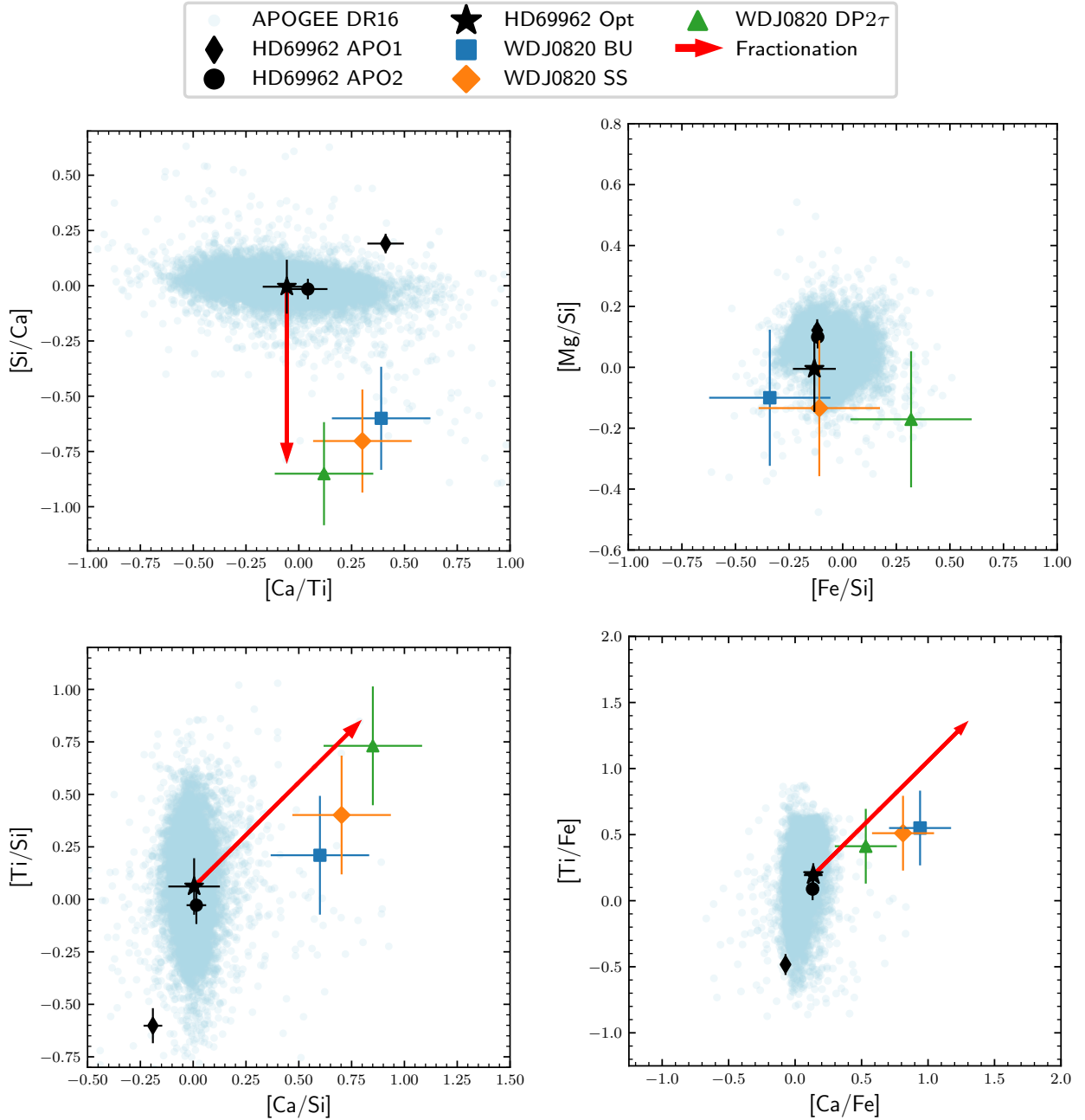


Fig. 5: Abundance ratios of different elements. Black points represent two APOGEE measurements without flags and our optical spectra measurement of HD69962 (with 1σ uncertainties as errorbars), contrasted against other stars in APOGEE (light blue). Most of our measurements are consistent with the bulk of the Galaxy. The white dwarf WDJ0820 abundances are depicted, considering potential phases of build-up (BU), steady state (SS) or declining phase after 2 sinking timescales of Mg (2τ). A red arrow illustrates the potential effect of incomplete condensation and how it modifies the abundance ratios of the primordial stellar nebula, although heating in the post-nebular phase would produce a similar effect to these elements. The size of the red arrows reflects the predicted effect on elemental abundances when the material is heated to 1340 K. Considering fractionation, the abundances of star and accreted planetary material are consistent within uncertainties.

3.2. The composition of planetary material from the abundances of the polluted white dwarf

The abundance ratios of various elements observed in the atmosphere of a white dwarf may differ to those in the accreted body due to the differential sinking of elements in the white dwarf atmosphere.

Polluted white dwarfs can be found and classified in three distinct phases of evolution, as depicted in Figure 1, in phases

from (E) to (G). In the build-up phase (E), accretion onto the white dwarf occurs without sufficient time for different elements to sink deeper into the atmosphere, remaining all visible in the atmosphere. Consequently, the measured abundances accurately reflect those of the engulfed material. Transitioning to the steady-state phase (F) in the evolution, the white dwarf continues to accrete material, but each element undergoes sinking at varying rates. During this phase, inferring the elemental ratio of

the accreted planet requires scaling the measured abundance by the respective sinking timescales. The final phase unfolds when the white dwarf ceases accretion (G). In this declining phase, elemental ratios decrease from the atmosphere exponentially, as each element progressively sinks without additional accretion.

As WD J0820 shows no evidence for current accretion, from infrared or gaseous emission, it is not clear whether accretion recently started, or indeed has finished. From optical spectroscopy, there is no evidence of circumstellar gas in emission or absorption, nor is there any sign of excess infrared emission from dust. Although there could be an undetected disc of gas/dust, it is less likely that the white dwarf is actively accreting from a disc.

Relative sinking creates a characteristic fingerprint in relative abundances of various elements, which contrasts with the fingerprint of processes that may have occurred to the planetary body before it was accreted by the white dwarf. Here, we assume that the abundances currently in the atmosphere come from a single body, or smaller chunk of a larger body. This body formed out of material that had the same composition as the star, HD69962. The planetary body formed may have experienced incomplete condensation and/or lost moderately refractories compared to the star. These moderately refractory and volatile elements may be depleted during formation, due to impact heating post-formation, whilst on the main-sequence, or due to volatile loss during stellar evolution. The planetary body may also have undergone the large scale melting that leads to the formation of an iron core, with subsequent accretion of material predominantly from the core (or mantle) by the white dwarf. We use a Bayesian framework to assess the most likely combination of relative sinking, depletion of volatiles and segregation into the iron melt during core formation that best describe the observed abundances.

This Bayesian model assesses the bulk chemistry of the planetary material accreted by the white dwarf, using the abundances of the main sequence star as a starting point. The effects of relative sinking are disentangled from those of planetary evolution by considering how multiple elements behave relative to each other. Distinct patterns in relative elemental abundances are associated with sinking, loss of volatiles, or the segregation of material into the iron melt that occurs during the formation of an iron core. This approach allows us to distinguish the individual consequences of each step, with a particular emphasis on exploring the impact of planet formation on planetary composition. By disentangling the processes involved, we gain a better understanding of how each factor contributes to the final composition of the planetary material.

The Bayesian framework was developed in (Harrison et al. 2018, 2021a; Buchan et al. 2022) and can be found on GitHub¹. We edited the framework in order to avoid situational unphysical behavior associated with condensation of refractory elements at extreme temperature. We increased the minimum formation distance such that the temperature could not exceed 1700K (~ 0.1 AU), and set the minimum possible Mg abundance to zero. For this work, unlike in previous studies where this had to be left as an unknown parameter, the initial abundances can be fixed to the abundances of the binary companion, HD69962. We use single values for the stellar abundances without considering the spread or sampling from the uncertainties. Although the errors in stellar composition are not negligible, they are considerably smaller than the uncertainties that would result from inferring the star's composition from the entire stellar population.

As a result of the Bayesian model applied, the most likely explanation for the observed abundances is accretion in the de-

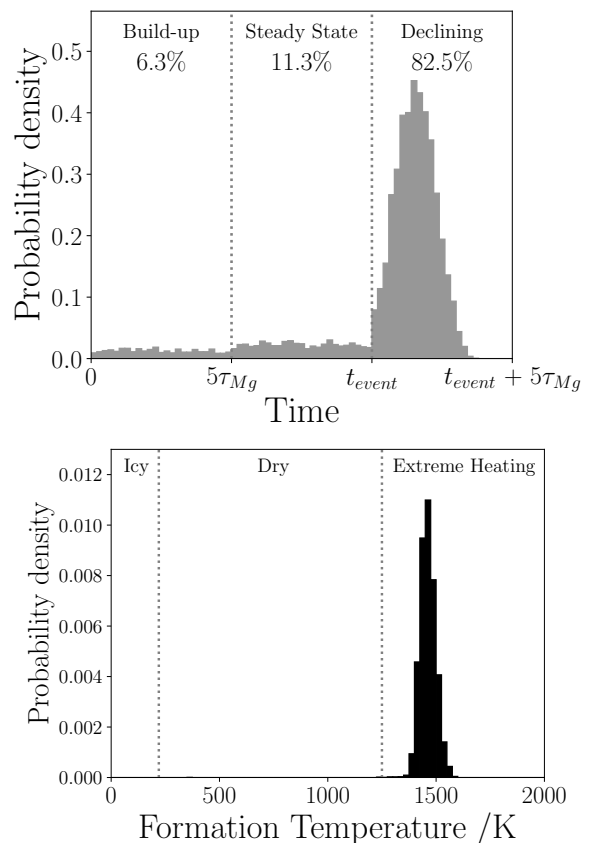


Fig. 6: Posterior distributions of the time since accretion started onto the white dwarf (top panel) and the formation temperature of the planetary material needed to explain its observed composition (bottom panel). In the top panel τ_{Mg} is the Mg sinking timescale and t_{event} represents the accretion event lifetime, indicating that the most probable explanation for the observed abundances is that the white dwarf is currently in the declining phase.

clining phase, involving material that is depleted in moderate refractories. This is illustrated in Figure 6, where the median time since accretion finished is $2.78^{+1.69}_{-3.98}$ Myr, and the required temperature to explain the observed depletion is $T = 1460^{+40}_{-30}$ K. This interpretation of the abundances is discussed in more detail in the following sections.

3.3. Sinking and WD accretion phase

In deriving planetary material abundances for the precursor accreted body from the polluted white dwarf, it is crucial to consider the impact of sinking. Figure 5 provides a depiction of the planetary material abundance in three potential phases of white dwarf accretion: build-up (BU), steady-state (SS), and declining phase (DP) using as a reference the sinking timescale of Mg (See Table 2). In other words, these are the abundances measured in the white dwarf corrected by the effects of sinking. We selected the Mg sinking timescale as a temporal reference for consistency, as elemental ratios are later expressed relative to Mg throughout the analysis. Although Fe is often used in stellar astronomy, it is less suitable here due to geological processes that could alter its composition in the planetesimal. Thus, Ca and Mg are considered better options, but Mg was ultimately chosen due to the relatively large Ca abundance observed in the white dwarf.

¹ https://github.com/andrewbuchan4/PyllutedWD_Public

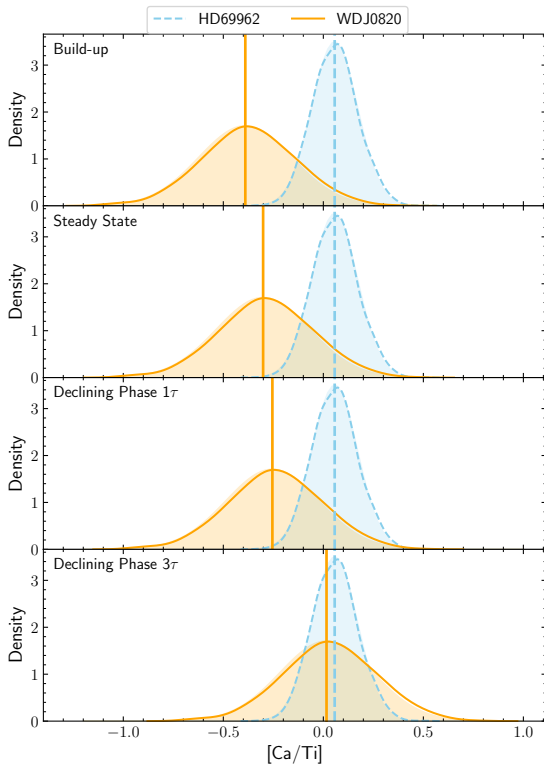


Fig. 7: $[\text{Ca}/\text{Ti}]$ abundance ratio distributions of the star HD69962 (blue dashed line) and its white dwarf companion WD J0820 (orange solid line). Different panels show the abundance of the white dwarf after being modified according to the accretion stage. From top to bottom we find build-up, steady state, declining phase after 1 and 3 sinking timescales of Mg (τ)

The key ratio for defining the accretion phase is predominantly $[\text{Ca}/\text{Ti}]$. Both Ca and Ti are refractory elements, the ratio of which is expected to remain unaffected by planet formation processes. Consequently, after correcting for the effects of sinking, the $[\text{Ca}/\text{Ti}]$ ratio should be consistent with that measured for the star. The observation that $[\text{Ca}/\text{Ti}]$ is higher in the white dwarf compared to the star implies that the most suitable phase to explain the ratio is DP, but SS cannot be ruled out given the uncertainties.

This can also be seen in Figure 7, which compares the $[\text{Ca}/\text{Ti}]$ distribution of the binary companion HD69962 with that of the planetary material, assuming build-up, steady state, declining phase after 1 Mg sinking timescale, and declining phase after 3 Mg sinking timescales. Although the match between binary companion and planetary material composition is reasonably good for any accretion phase, considering the substantial uncertainties in the measurements, the distributions progressively converge, particularly in SS and DP. However, while the $[\text{Ca}/\text{Ti}]$ ratio can provide insights into a specific accretion phase, a comprehensive assessment of the accretion phase requires considering other elemental ratios to determine the best fit that explains all the compositional data obtained for the white dwarf simultaneously.

As seen in Table 2, Mg and Si exhibit similar sinking timescales, i.e., diffusion timescales, suggesting that the $[\text{Mg}/\text{Si}]$ ratio should undergo minimal changes due to settling. This expectation aligns with the observed slight variation in the top-right panel of Figure 5, where $[\text{Mg}/\text{Si}]$ remains consistent between BU, SS, and DP, closely mirroring the $[\text{Mg}/\text{Si}]$ ratio of

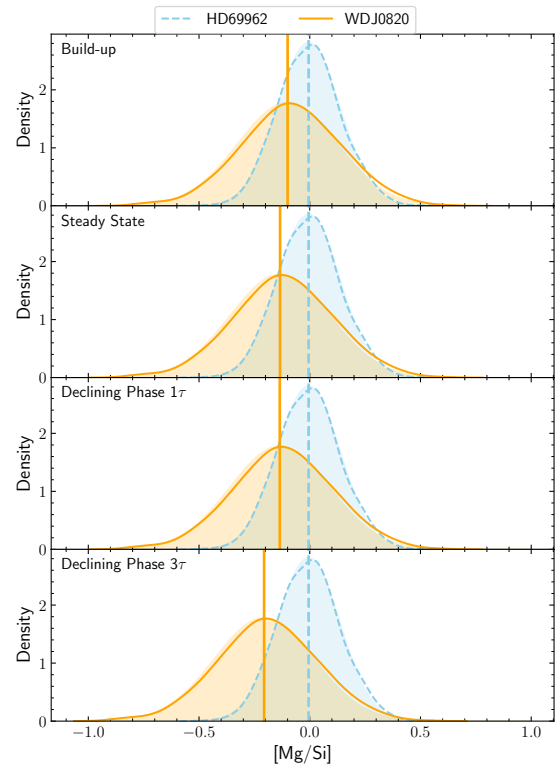


Fig. 8: $[\text{Mg}/\text{Si}]$ abundance ratio distributions of the star HD69962 (blue dashed line) and its white dwarf companion WD J0820 (orange solid line). Different panels show the abundance of the white dwarf after being modified according to the accretion stage. From top to bottom we find build-up, steady state, declining phase after 1 and 3 sinking timescales of Mg (τ).

the star within uncertainties. We notice that this ratio is closer to the abundances measured in the optical than APOGEE, but still consistent, regardless of the selected dataset.

Further confirmation of the lack of change in $[\text{Mg}/\text{Si}]$ for the white dwarf accretion phase is illustrated in Figure 8. The distribution of the star and planetary material is consistent with every accretion phase alike, given that the observed changes are significantly smaller than those detected for the ratio of refractory elements.

The role of Fe is key in this context due to its faster sinking rate compared to Mg and Si, despite sharing a similar condensation temperature (Lodders 2003). Note that when estimating the parent body abundance from the white dwarf's current accretion phase, the difference in sinking rates (Fe sinking faster than Mg and Si) causes estimated abundance ratios such as $[\text{Mg}/\text{Fe}]$, to decrease from BU to SS and then to DP, as shown in the equations in Figure 1.

The planetary ratios $[\text{Mg}/\text{Fe}]$ and $[\text{Si}/\text{Fe}]$ experience substantial changes across different phases of white dwarf accretion, providing valuable insights into the system. Distributions of these ratios in the star, alongside corrected ratios for planetary material derived from the white dwarf abundance, are presented in Figures 9 and 10. Analysis of these ratios strongly indicates that the optimal match occurs in the transition between the SS and the initial DP, excluding the possibility of an extended declining phase duration given that after accounting for sinking timescales, the abundance ratio of planetary material becomes notably smaller than that of the star, indicating inconsistency. The comprehensive analysis of all ratios collectively supports

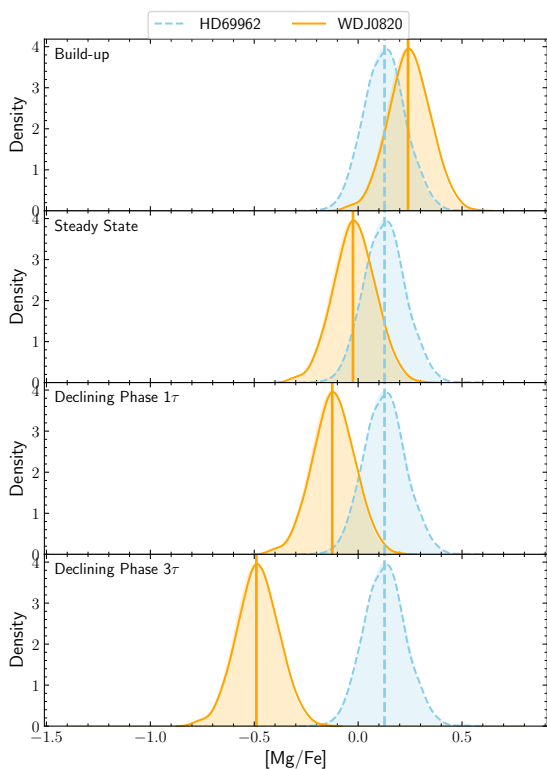


Fig. 9: $[\text{Mg}/\text{Fe}]$ abundance ratio distributions of the star HD69962 (blue dashed line) and its white dwarf companion WDJ0820 (orange solid line). Different panels show the abundance of the white dwarf after being modified according to the accretion stage. From top to bottom we find build-up, steady state, declining phase after 1 and 3 sinking timescales of Mg (τ)

the conclusion that the accretion phase most consistent with the observed chemistry of the planetary material is the beginning of the declining phase.

An important conclusion can be deduced from these presented ratios. Grouping elements based on their condensation temperature reveals a distinct pattern. Elements such as Mg, Si, and Fe, characterized by moderately refractory properties, share similar condensation temperatures. In contrast, Ca and Ti, deemed refractory elements, exhibit higher condensation temperatures. When grouping elements by condensation temperature, they consistently maintain the abundance of the star. In other words, instead of considering the abundance of each element independently, we analyze the ratios of elements with similar condensation temperatures. The relative abundances of these grouped elements are expected to be roughly the same as those in the star. This observation shows a fundamental principle: any process influencing the planetary composition will produce a similar effect on elements with similar condensation temperatures. Therefore, when elements are categorized according to this characteristic, they consistently mirror the star's abundance.

While the already discussed ratios ($[\text{Ca}/\text{Ti}]$, $[\text{Mg}/\text{Si}]$, and $[\text{Mg or Si}/\text{Fe}]$) demonstrate consistency, Figure 5 highlights the contrast in other element combinations. For instance, $[\text{Si}/\text{Ca}]$ in the top-left panel, $[\text{Ti}/\text{Si}]$ in the bottom-left panel, and $[\text{Ti}/\text{Fe}]$ and $[\text{Ca}/\text{Fe}]$ in the bottom right, all exhibit considerable differences from the stellar composition. This holds true even when considering only the previously determined accretion phase for the white dwarf (DP) and accounting for the large uncertain-

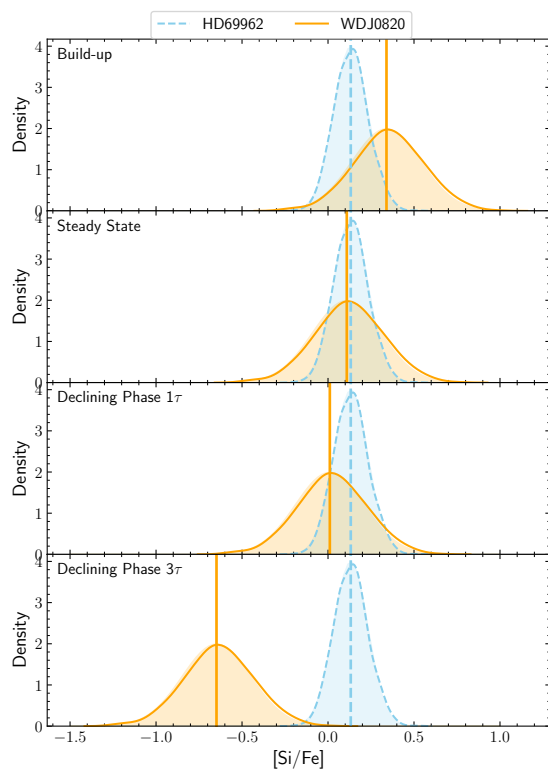


Fig. 10: $[\text{Si}/\text{Fe}]$ abundance ratio distributions of the star HD69962 (blue dashed line) and its white dwarf companion WDJ0820 (orange solid line). Different panels show the abundance of the white dwarf after being modified according to the accretion stage. From top to bottom we find build-up, steady state, declining phase after 1 and 3 sinking timescales of Mg (τ)

ties in the abundances. These inconsistencies for certain ratios suggest that only considering sinking effects is insufficient to explain the chemical composition of the planetary material. Instead, it strongly implies that additional processes must be at play during the planet formation stage, affecting the abundances and introducing variations from the primordial composition inherited from the star.

3.4. Effects of planet formation on the composition of planetary material

We can focus on the elemental abundance ratios exhibiting disparities. For instance, the $[\text{Si}/\text{Ca}]$ ratio is notably higher in the star compared to the planetary material (indicated by the triangle symbol in Figure 5), whereas ratios such as $[\text{Ti}/\text{Si}]$ or $[\text{Ca}/\text{Fe}]$ are lower. Given that the accreted body is enriched in refractory elements and mirrors the abundance of the star, this discrepancy suggests a significant depletion of Si from the primordial composition. A similar analysis of other ratios reveals a consistent depletion of Si, Fe, and Mg from the stellar abundance, indicative of the loss of moderately refractory elements, consistent with a heating process, or depletion due to incomplete condensation. In this section, we consider that planetary bodies may display varying elemental ratios due to the incomplete condensation of nebula gas during grain growth in the protoplanetary disc.

The effect of incomplete condensation on chemical composition is shown in Figure 5 as a red arrow, originating from the measured stellar abundance. The size of this arrow, i.e., how

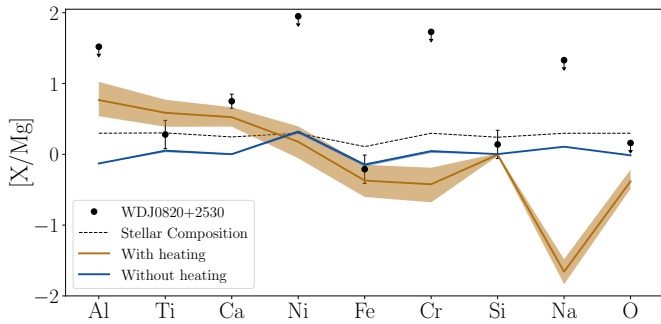


Fig. 11: Comparison of abundances of WD and the main sequence star using optical data. Abundances are shown relative to Mg, and normalised to Solar composition on a log scale. The model with the highest Bayesian evidence, which includes heating, is shown in orange. This model also includes a feeding zone. The best model which does not include heating is shown in blue. This model cannot fit the data well, and so is heavily disfavoured. The small confidence interval for the non-heating model is due to its limited number of free parameters, mostly fixed or tightly constrained.

much the primordial composition changes, depends on the extent of fractionation endured by the planetary material. As such, we can interpret its direction as a guide to anticipate the expected changes in abundance. Notably, the tip of the arrow corresponds to a temperature of the disc of approximately ~ 1340 K, similar to the temperature estimate from the Bayesian model in Sect. 3.2. For all combinations of elements presented, the measured abundance for the planetary material (indicated by the triangle symbol) aligns consistently with the primordial abundance (represented by the star symbol) plus heating in the direction of the arrow. Although the effect of this arrow considers incomplete condensation, for the elements Mg, Si, Fe, Ti, and Ca, the impact should be similar to that of post-nebular volatilization. However, this similarity does not hold for volatile or moderately volatile elements such as Na and Mn, which exhibit different trends depending on whether they are affected before or after the dissipation of the nebula (Harrison et al. 2021b).

The influence of fractionation or heating is consistent with the optimal solution identified through the Bayesian framework, as depicted in Figure 11. This shows the measurements of the white dwarf (represented by points) and its stellar companion (illustrated by the dashed line), and fits that represent the posterior distribution derived from the Bayesian analysis, accounting for the effects of sinking. The model lacking heating (Figure 11, blue line) maintains consistency in $[\text{Fe}/\text{Mg}]$ and $[\text{Si}/\text{Mg}]$ ratios but inadequately explains the abundance Ti and Ca. Conversely, the model incorporating heating appropriately accounts for the elevated Ca abundance observed in the white dwarf while also capturing the variations in moderately refractory elements. The elements Al, Cr, Na and O would provide additional constraints on the model, but presently we only have upper limits for their abundances: these upper limits are consistent with the model result.

4. Discussion

In this section, we evaluate at what point in the system’s evolution the exoplanetary material experienced elemental fractionation. We also consider alternative explanations for a possible

heating source and discuss the assumptions involved in analyzing abundance data for main sequence star and white dwarf.

4.1. Element fractionation during planet formation

The first major stage of element fractionation occurs due to the incomplete condensation of gas as the protoplanetary disc cools.

Models, such as those proposed by Chambers (2009), establish temperature and pressure conditions within the protoplanetary disc based on the characteristics of the host star. This enables the estimation of the fraction of an element in its solid state relative to its gaseous state at specific times and locations along the disc (Harrison et al. 2018). Such modeling can be tailored to any particular star and is consistent with the condensation temperatures reported for the Solar System, as derived from Solar photospheric abundances and meteorite measurements (e.g., Lodders 2003). Accordingly, elements such as Ca and Ti are expected to condense at approximately 1400 K, whereas moderately refractory elements like Mg, Si, and Fe condense at around 1300 K. Consequently, based on our results from Section 3, we can approximate the temperature of formation for the planetary material to lie between these two condensation temperatures.

To estimate at which point in the disc we find this temperature, we must first estimate the mass of the white dwarf progenitor. Since both stars in the binary system are coeval, the progenitor must have been more massive than HD69962 to reach the white dwarf stage. This sets a lower limit for the progenitor mass, indicating that the disc temperature exceeds that of a Solar-type star due to the stars’ initially higher mass. Using *wdwarfdate* (Kiman et al. 2022), we derive the progenitor’s mass based on the white dwarf’s effective temperature and surface gravity, employing evolutionary sequences from Bédard et al. (2020), with thin outer hydrogen layers. Additionally, the code requires the use of an initial to final mass relation. We use relations provided by Cummings et al. (2018) or Marigo et al. (2020), resulting in estimated progenitor masses ranging from $\sim 1.4 - 1.5 M_{\odot}$ with uncertainties around $0.5 M_{\odot}$. Changing the metallicity of the system alters the estimated mass slightly, but always within the given uncertainties. This calculation suggests that the white dwarf progenitor is a late A type star, despite significant uncertainties.

Assuming a white dwarf progenitor mass of $1.5 - 1.6 M_{\odot}$ and using MESA evolutionary models, it’s estimated that a planetary body must have an initial semi-major axis of at least ~ 1.0 au to survive stellar evolution. However, a planetary body at such distances would not reach the ~ 1400 K necessary to explain the observed abundance ratios during its formation or the main sequence phase of its host star. To reach this temperature the body would need to be closer to the star, at ≤ 0.5 au initially, conflicting with the survival threshold of ≥ 1.0 au. This implies that either energetic collisions or radiogenic heating during the pre-main sequence or early main sequence phase, would be required to heat the planetary body if it is located at 1.0 au or more. Note that the distance from the star required to reach the necessary temperature could be extended outward when considering more complex structures for the disc and accounting for accretion heating of the protoplanetary disc (e.g., Ueda et al. 2023). While heating during the asymptotic giant branch phase could contribute, our analysis suggests it’s unlikely to produce the observed elemental ratios (see Section 4.3.1). Alternatively, if the planetary body starts at 0.5 au, it must migrate outward to a safe distance before the host star experiences thermal pulsations. These presented semi-major axis estimates are dependent on the model and formation time, but they provide useful references.

Although our estimate of the star mass is uncertain, even increasing it up to $3.5 M_{\odot}$ does not change our conclusion: Higher main-sequence temperature would push the location where the planetesimal experiences 1400 K farther away from the star, but since the maximum radius of the star during the AGB also increases with mass, the body would have to migrate beyond 2.0 au to survive. Thus, regardless of the star's mass, the challenge is the same: A planetary body in close initial proximity to the star that experiences enough heating, conflicts with survival thresholds that would allow it to be accreted during the white dwarf phase.

In conclusion, elemental fractionation of the material polluting the white dwarf needed to happen early. Either the depletion of moderately refractories could have occurred during nebular condensation, followed by planetary body migration to a safer orbital distance to the star, or moderately refractory loss may have happened during the post-nebular phase via impacts and spontaneous isotope disintegration.

4.2. Assumptions and limitations

4.2.1. Main sequence star abundance determination uncertainties

It is worth discussing the impact of our results on the uncertainties of the measured abundances in the main sequence star. The fact that HD69962 has substantial spectral line broadening produced by its rotation induces higher uncertainties in the abundances measured. The significant broadening, causes higher levels of blending with other lines, which can contaminate the abundance of some elements because of the absorption caused by the elements of neighboring lines. In broad lines it is also harder to accurately identify the level of the continuum. Nonetheless, as demonstrated by [Casamiquela et al. \(2022\)](#), our method is still able to synthesize broad lines and determine consistent abundances for stars rotating as fast as HD69962. After a careful revision of the line-by-line fits we selected only the lines that presented good fits. Additionally, we selected only the lines which have shown to yield trustworthy results in the literature.

We can validate our results by comparing our abundances to those of APOGEE DR16, which provides independent measurements for three different spectra of the star. This is however an unfair comparison because APOGEE is focused on a different spectral range (thus other spectral lines) and the APOGEE pipeline has been optimized to work with red giants which rotate slow.

Abundance ratio of [Si/Fe] is consistent among these 3 measurements and our own, despite the APOGEE Flag for that measurement about "Parameter in possibly unreliable range of calibration determination". Our measurement of [Ti/Fe] of 0.193 agrees, within the uncertainties, only with one of the two measurements of APOGEE. While no flag is reported in APOGEE, the highly discrepant measurements hint to a very uncertain measurement, probably not recommended for validation with our result. Indeed, as concluded by [Jönsson et al. \(2020\)](#), Ti measurements should be treated with caution in APOGEE DR16.

Regarding [Ca/Fe], our result agrees with only one from APOGEE. This measurement only reports a warning for the measurement of APO3, which has the flag "Parameter in possibly unreliable range of calibration determination". Considering distributions of abundances in the Milky Way, it is expected that alpha-capture elements have comparable levels of enhancement with respect to Fe in a star. The fact that Ca, Ti and Si are all between 0.1 and 0.2 dex is another hint toward the accuracy of

our measurements. The difference of the Ca abundance between HD69962 and the white dwarf cannot be attributed to a wrong abundance measurement of the main sequence star.

The abundance of [Mg/Fe], among the alpha-capture elements studied here, is the most difficult to determine. The two best lines in the optical for a large variety of stars are 613.8 and 613.9 nm (see discussion in e.g., [Jofré et al. 2015, 2019](#)) and are blended in HD69962. The only line left with good fits presented is the 552.84 nm, which in [Heiter et al. \(2021\)](#) was reported to be a good line for synthesis, but its atomic data quality was undetermined. The [Mg/Fe] abundance is obtained only from that line and while it is a bit lower than all three APOGEE values, is still within the uncertainties, and still consistent with Si, Ca and Ti.

The measurements of [Cr/Fe] and [Na/Fe] agree well with APOGEE, but [Ni/Fe] disagrees by 0.2 dex, although our measurement has high uncertainties. Considering that [Jönsson et al. \(2020\)](#) concludes that Ni is among the best elements in APOGEE, and that our value of [Ni/Fe] of 0.4 is higher than the expected distributions of normal stars in the solar neighborhood, it is possible that our value is not correct. After removing lines with bad flags in the atomic data from [Heiter et al. \(2021\)](#), we used 7 lines for our measurement. Among these lines, only two of them (542.4 and 600.7 nm) have Y flags in [Heiter et al. \(2021\)](#), indicating they are good to be used to measure abundances with spectral synthesis, and the abundances of these two lines are of the order of 0.5 dex. We do not aim to understand the nature of this enhancement, because this value is still lower than the upper limit estimated to the white dwarf, making the abundances of this element not a key player in our conclusions.

4.2.2. Uncertainties in white dwarf measurements and atmospheric modeling

As is the case of the main sequence star, measuring the element abundance from the white dwarf and then tracing it back to a possible planetary composition relies on a series of assumptions, that affect our results. One fundamental assumption is that the pollution of the white dwarf is produced through accretion from a single planetary body, although this may not hold true in all instances ([Turner & Wyatt 2020; Johnson et al. 2022](#)).

The scarcity of spectral lines in white dwarfs implies a significant challenge, not only because the measurement needs to be made with fewer spectral features but also due to potential uncertainties in the atomic data of these lines.

On the other hand, transforming measured abundances into elemental ratios in the planetary material relies on the modeling of the white dwarf's atmosphere and the settling timescales that can remove those observed heavy elements from sight. Given that white dwarfs in the temperature regime where we find WD J0820 have developed convective zones, the treatment of convection within the region and overshooting into the diffusion-dominated region below becomes crucial for understanding planetary material accretion. However, conventional 1D models, like those used in this study, apply the mixing length theory for convection and may underestimate the sinking timescales and the extent of mixing beyond the bottom of the convective layer, as exemplified by [Cunningham et al. \(2019\)](#) using 3D models of DA white dwarfs. This emphasizes the importance of incorporating a comprehensive treatment of white dwarf atmospheres in 3D, including effects such as overshooting, to mitigate potential biases in the measured planetary abundance ratios.

4.3. Alternative explanations for the composition of the planetary material

4.3.1. Asymptotic Giant Branch heating

While moderately refractory element depletion can occur during the nebular phase due to incomplete condensation, it is also plausible for the planetary material to undergo compositional changes at later stages. In the post-nebular phase, radioactive decay and collisions may lead to melting and vaporization of species (Siebert et al. 2018), as mentioned in Section 4.1. Alternatively, during the stellar evolution of the host star, particularly in the asymptotic giant branch phase, the planetary material may be subjected to heating by the star (Li et al. 2024).

Exoplanetary material engulfed by a white dwarf must endure the star’s entire evolution, including dynamic interactions that may lead to migration, engulfment, or disruption. It is crucial to accurately model the stellar and orbital evolution to understand the survivability limits of planets. Moreover, stellar irradiation can mimic processes that happen during planet formation. As such, understanding the thermal evolution of a planet allows us to evaluate whether heating can melt the outer portion of the body, inducing a loss in moderately refractory elements even before reaching the white dwarf phase. Given that core-mantle differentiation and asynchronous accretion can affect elemental ratios such as Si/Fe or Ca/Fe (Brouwers et al. 2023), it is relevant to test if late-stage thermal evolution of the exoplanetary material could produce the signals we found in this system. Studies by Li et al. (2024) suggest that known pollutants found in helium-dominated white dwarfs are unlikely to be differentiated during the star’s giant branch phases. An estimation using the specific parameters of this system reveals a similar conclusion.

Estimating the mass of planetary material needed to create the observed signature ($\sim 3 \times 10^{21}$ kg) and assuming a density of 3–8 g/cm³, we find that the accreted body’s radius is about 400–600 km. During the star’s giant branch phases, the heating effects are significant but the duration is insufficient for substantial thermal penetration beyond the planetesimal’s surface layer. The diffusion length scale remains too small to impact anything beyond the surface, as supported by numerical evidence (e.g., Li et al. 2024). Optimistically, a surface layer less than ~ 20 km may undergo moderately refractory depletion. Thus, it’s unlikely that the observed moderately refractory depletion in the white dwarf pollutant was caused by heating during the giant phases of stellar evolution.

4.3.2. Crust accretion

An alternate explanation for the high Ca, Ti abundances of the planetary material accreted by WD J0820 is that the material present in the atmosphere currently is the crust of a planetary body. Crustal material has undergone further phases of successive melting and would be enhanced in elements such as Ca and Ti, but also Al. Na is a crucial element with the potential to distinguish between crustal material and material that has undergone successive heating. Unfortunately Na is not detected in the spectrum of WD J0820 and the Na upper limit does not distinguish between crust and loss of moderate volatiles.

The abundances of WD J0820 were compared to both crustal material and Lunar anorthosite, a very Ca-rich rock (see Figure 12). However, the Ca/Si ratio of the white dwarf is not in agreement with the abundance of either material. Invoking the accretion of continental crust to explain the observed abundances would add extra complexity to the model, such as requiring se-

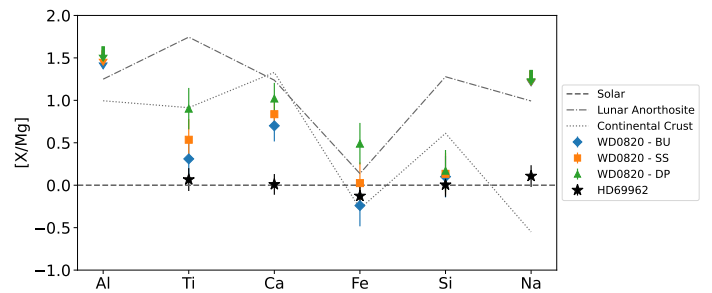


Fig. 12: Comparison of the main sequence and white dwarf abundances in different accretion phases, including the typical composition of continental crustal material (dotted line) and Lunar anorthosite (dot-dashed lines). These abundances are normalized to Solar values. Downward arrows in this figure represent the upper limits measured in the white dwarf atmosphere.

lective accretion of the planetary material’s surface rather than the entire body. Therefore, with the current available data, there is no reason to suggest that these are more likely explanations. The sodium abundance would act as a potential discriminator between crustal sodium-rich material and material depleted in moderate volatiles due to heating, which is sodium poor. The current upper limit on Na does not discriminate between the two scenarios.

4.3.3. Primordial Cloud

In this work, we have assumed that both stars in the binary system and the planet formed from the same cloud of gas and dust. However, the homogeneity of such clouds remains debated (e.g. Ramírez et al. 2019). The discovery of a comoving pair with significant compositional differences, such as Kronos and Krios (Oh et al. 2018; Miquelarena et al. 2024), including important discrepancies in their metallicities, suggests that the original cloud might not have been homogeneous. Alternatively, other processes, such as planet engulfment (Spina et al. 2021) or atomic diffusion (Liu et al. 2021), could have altered the abundance of one of the stars. Saffe et al. (2024) identified a wide binary pair of giant stars with a difference in composition of 0.073 ± 0.035 dex for volatile elements and 0.081 ± 0.010 dex for refractories, potentially indicating a primordial origin for such discrepancies. This finding implies that wide binaries might not always share identical abundances. Most wide binaries exhibit metallicity differences smaller than $\Delta[\text{Fe}/\text{H}] = 0.1$ dex between components (e.g. Behrard et al. 2023). This difference falls within the error bars of our stellar composition measurements. Therefore, the depletion of mildly refractory elements observed in this study is unlikely to be explained by compositional differences between the F-star and the planet-forming material, though this possibility cannot be entirely excluded.

5. Conclusions

To understand the interior composition of exoplanets, one common approach is to assume that planets share the composition of their host stars, as both originate from the collapse of the same primordial cloud. However, it is important to investigate how the planet formation process modifies the composition of the nebula.

Spectroscopy of polluted white dwarfs provides the composition of the exoplanetary material they have accreted. When these white dwarfs are part of a wide binary system, they provide

a unique opportunity to compare stellar and planetary compositions. Assuming chemical homogeneity within wide binaries, the companion composition serves as a proxy for the nebula's abundance, from which both stars and planets formed.

Following the work by [Bonsor et al. \(2021\)](#), who used one of these systems to confirm that the refractory composition of a planet and its host star match, we present the second paper in our series. In this study, we introduce a new wide binary system with a polluted white dwarf and a main sequence companion, exploring the link between host-star and planetary abundances.

We present detailed abundances of Fe, Mg, Si, Ca, and Ti for both white dwarf and its companion, a main-sequence F-type star. The companion is used to fix the initial conditions for the entire system, including the white dwarf's progenitor. After considering the effects of sinking in the white dwarf's atmosphere, we derive the abundance of the accreted planetary material.

The key results of our work are summarized as follows:

- Consistent initial composition: The abundances of the accreted planetary material, as seen in the white dwarf atmosphere are consistent with planet formation starting from the same initial abundances as its host star.
- Moderate refractories depletion: Before arrival onto the white dwarf the planetary material is depleted in moderate refractories, including Mg, Si and Fe, relative to refractory elements (Ca, Ti, Al). This depletion follows the relative volatility of elements, as characterised by their condensation temperatures.
- Using condensation temperatures: Grouping elements by condensation temperature provides an effective diagnostic for linking planet-host star and planet composition.
- Possible causes of depletion: The lack of moderately refractory species in the accreted planetary material by the white dwarf could have occurred due to incomplete condensation, heating during planet formation or subsequent migration, radiogenic heating, collisions or indeed during the evolution onto the white dwarf.

This work highlights the best means to utilise stellar compositions to inform our understanding of planetary compositions. Future observations of polluted white dwarfs in wide binary systems with multiple elements and different histories will improve the determination of interior compositions of rocky exoplanets and help understanding the intricacies of the planet formation process.

Acknowledgements. This work uses observations obtained through a Chilean Telescope Allocation Committee (CNTAC) proposal under ID CN2021B-56. We thank the referee for their valuable comments and suggestions, which have helped improve the clarity and quality of this work. C.A.G. acknowledges support from Agencia Nacional de Investigación y Desarrollo (ANID), Proyecto FONDECYT Iniciación 11230741. C.A.G and P.J. acknowledges support from ANID Proyecto FONDECYT Regular 1231057 and Millennium Nucleus ERIS NCN2021_017. LKR acknowledges support of an ESA Co-Sponsored Research Agreement No. 4000138341/22/NL/GLC/my = Tracing the Geology of Exoplanets. AB and LKR acknowledges the support of a Royal Society University Research Fellowship, URF\R1\211421. AMB acknowledges the support of a Leverhulme Trust Grant (ID RPG-2020-366). S.X. is supported by the international Gemini Observatory, a program of NSF's NOIRLab, which is managed by the Association of Universities for Research in Astronomy (AURA) under a cooperative agreement with the National Science Foundation on behalf of the Gemini partnership of Argentina, Brazil, Canada, Chile, the Republic of Korea, and the United States of America.

References

Adibekyan, V., Dorn, C., Sousa, S. G., et al. 2021, *Science*, 374, 330
Anders, E. & Ebihara, M. 1982, *Geochim. Cosmochim. Acta*, 46, 2363

Andrews, J. J., Anguiano, B., Chanamé, J., et al. 2019, *ApJ*, 871, 42
Bédard, A., Bergeron, P., Brassard, P., & Fontaine, G. 2020, *ApJ*, 901, 93
Behrard, A., Dai, F., Brewer, J. M., Berger, T. A., & Howard, A. W. 2023, *MNRAS*, 521, 2969
Bernstein, R., Shectman, S. A., Gunnels, S. M., Mochnacki, S., & Athey, A. E. 2003, in *Society of Photo-Optical Instrumentation Engineers (SPIE) Conference Series*, Vol. 4841, *Instrument Design and Performance for Optical/Infrared Ground-based Telescopes*, ed. M. Iye & A. F. M. Moorwood, 1694–1704
Blanco-Cuaresma, S. 2019, *MNRAS*, 486, 2075
Blanco-Cuaresma, S., Soubiran, C., Heiter, U., & Jofré, P. 2014, *A&A*, 569, A111
Blouin, S., Dufour, P., & Allard, N. F. 2018, *ApJ*, 863, 184
Bonsor, A., Jofré, P., Shorttle, O., et al. 2021, *MNRAS*, 503, 1877
Brouwers, M. G., Bonsor, A., & Malamud, U. 2023, *MNRAS*, 519, 2646
Buchan, A. M., Bonsor, A., Shorttle, O., et al. 2022, *MNRAS*, 510, 3512
Casamiquela, L., Gebran, M., Agüeros, M. A., Bouy, H., & Soubiran, C. 2022, *AJ*, 164, 255
Chambers, J. E. 2009, *ApJ*, 705, 1206
Choi, J., Dotter, A., Conroy, C., et al. 2016, *ApJ*, 823, 102
Coutu, S., Dufour, P., Bergeron, P., et al. 2019, *ApJ*, 885, 74
Cummings, J. D., Kalirai, J. S., Tremblay, P. E., Ramirez-Ruiz, E., & Choi, J. 2018, *ApJ*, 866, 21
Cunningham, T., Tremblay, P.-E., Freytag, B., Ludwig, H.-G., & Koester, D. 2019, *MNRAS*, 488, 2503
Cunningham, T., Wheatley, P. J., Tremblay, P.-E., et al. 2022, *Nature*, 602, 219
Dorn, C., Khan, A., Heng, K., et al. 2015, *A&A*, 577, A83
Dufour, P., Bergeron, P., Liebert, J., et al. 2007, *ApJ*, 663, 1291
Dufour, P., Kilic, M., Fontaine, G., et al. 2012, *ApJ*, 749, 6
El-Badry, K. & Rix, H.-W. 2018, *MNRAS*, 480, 4884
El-Badry, K., Rix, H.-W., & Heintz, T. M. 2021, *MNRAS*, 506, 2269
Espinoza-Rojas, F., Chanamé, J., Jofré, P., & Casamiquela, L. 2021, *ApJ*, 920, 94
Farihi, J. 2016, *New A Rev.*, 71, 9
Gänsicke, B. T., Marsh, T. R., Southworth, J., & Rebassa-Mansergas, A. 2006, *Science*, 314, 1908
Gänsicke, B. T., Schreiber, M. R., Toloza, O., et al. 2019, *Nature*, 576, 61
Genest-Beaulieu, C. & Bergeron, P. 2019, *ApJ*, 882, 106
Gentile Fusillo, N. P., Gänsicke, B. T., & Greiss, S. 2015, *MNRAS*, 448, 2260
Grevesse, N., Asplund, M., & Sauval, A. J. 2007, *Space Sci. Rev.*, 130, 105
Guidry, J. A., Vanderbosch, Z. P., Hermes, J. J., et al. 2021, *ApJ*, 912, 125
Gustafsson, B., Edvardsson, B., Eriksson, K., et al. 2008, *A&A*, 486, 951
Harrison, J. H. D., Bonsor, A., Kama, M., et al. 2021a, *MNRAS*, 504, 2853
Harrison, J. H. D., Bonsor, A., & Madhusudhan, N. 2018, *MNRAS*, 479, 3814
Harrison, J. H. D., Shorttle, O., & Bonsor, A. 2021b, *Earth and Planetary Science Letters*, 554, 116694
Hawkins, K., Lucey, M., Ting, Y.-S., et al. 2020, *MNRAS*, 492, 1164
Hegedűs, V., Mészáros, S., Jofré, P., et al. 2023, *A&A*, 670, A107
Heiter, U., Jofré, P., Gustafsson, B., et al. 2015, *A&A*, 582, A49
Heiter, U., Lind, K., Bergemann, M., et al. 2021, *A&A*, 645, A106
Jofré, P., Heiter, U., & Soubiran, C. 2019, *ARA&A*, 57, 571
Jofré, P., Heiter, U., Soubiran, C., et al. 2015, *A&A*, 582, A81
Jofré, P., Heiter, U., Soubiran, C., et al. 2014, *A&A*, 564, A133
Johnson, T. M., Klein, B. L., Koester, D., et al. 2022, *ApJ*, 941, 113
Jönsson, H., Holtzman, J. A., Allende Prieto, C., et al. 2020, *AJ*, 160, 120
Jura, M. 2003, *ApJL*, 584, L91
Kelson, D. D. 2003, *PASP*, 115, 688
Kelson, D. D., Illingworth, G. D., van Dokkum, P. G., & Franx, M. 2000, *ApJ*, 531, 159
Kepler, S. O., Pelisoli, I., Koester, D., et al. 2015, *MNRAS*, 446, 4078
Kiman, R., Xu, S., Faherty, J. K., et al. 2022, *AJ*, 164, 62
Klein, B. L., Doyle, A. E., Zuckerman, B., et al. 2021, *ApJ*, 914, 61
Koester, D., Gänsicke, B. T., & Farihi, J. 2014, *A&A*, 566, A34
Koester, D., Kepler, S. O., & Irwin, A. W. 2020, *A&A*, 635, A103
Koester, D., Voss, B., Napiwotzki, R., et al. 2009, *A&A*, 505, 441
Li, Y., Bonsor, A., & Shorttle, O. 2024, *MNRAS*, 527, 1014
Liu, F., Bitsch, B., Asplund, M., et al. 2021, *MNRAS*, 508, 1227
Lodders, K. 2003, *ApJ*, 591, 1220
Marigo, P., Cummings, J. D., Curtis, J. L., et al. 2020, *Nature Astronomy*, 4, 1102
Miquelarena, P., Saffe, C., Flores, M., et al. 2024, *A&A*, 688, A73
Oh, S., Price-Whelan, A. M., Brewer, J. M., et al. 2018, *ApJ*, 854, 138
Ramírez, I., Khanal, S., Lichon, S. J., et al. 2019, *MNRAS*, 490, 2448
Rogers, L. K., Bonsor, A., Xu, S., et al. 2024, *MNRAS*, 527, 6038
Saffe, C., Miquelarena, P., Alacoria, J., et al. 2024, *A&A*, 682, L23
Seager, S., Kuchner, M., Hier-Majumder, C. A., & Militzer, B. 2007, *ApJ*, 669, 1279
Siebert, J., Sossi, P. A., Blanchard, I., et al. 2018, *Earth and Planetary Science Letters*, 485, 130
Snedden, C. A. 1973, PhD thesis, University of Texas, Austin
Soubiran, C., Creevey, O. L., Lagarde, N., et al. 2024, *A&A*, 682, A145
Spina, L., Sharma, P., Meléndez, J., et al. 2021, *Nature Astronomy*, 5, 1163
Swan, A., Farihi, J., Melis, C., et al. 2023, *MNRAS*, 526, 3815
Thiabaud, A., Marboeuf, U., Alibert, Y., Leya, I., & Mezger, K. 2015, *A&A*, 580, A30
Turner, S. G. D. & Wyatt, M. C. 2020, *MNRAS*, 491, 4672
Ueda, T., Okuzumi, S., Kataoka, A., & Flock, M. 2023, *A&A*, 675, A176
Vanderburg, A., Johnson, J. A., Rappaport, S., et al. 2015, *Nature*, 526, 546
Veras, D. 2016, *Royal Society Open Science*, 3, 150571
Wang, H. S., Lineweaver, C. H., & Ireland, T. R. 2018, *Icarus*, 299, 460
Wang, H. S., Liu, F., Ireland, T. R., et al. 2019, *MNRAS*, 482, 2222
Xu, S., Zuckerman, B., Dufour, P., et al. 2017, *ApJL*, 836, L7

Appendix A: WD spectrum

Figure A.1 shows key lines in the WD SDSS observed spectrum (gray), as labeled, alongside the best fit model (red line) in 4 different regions.

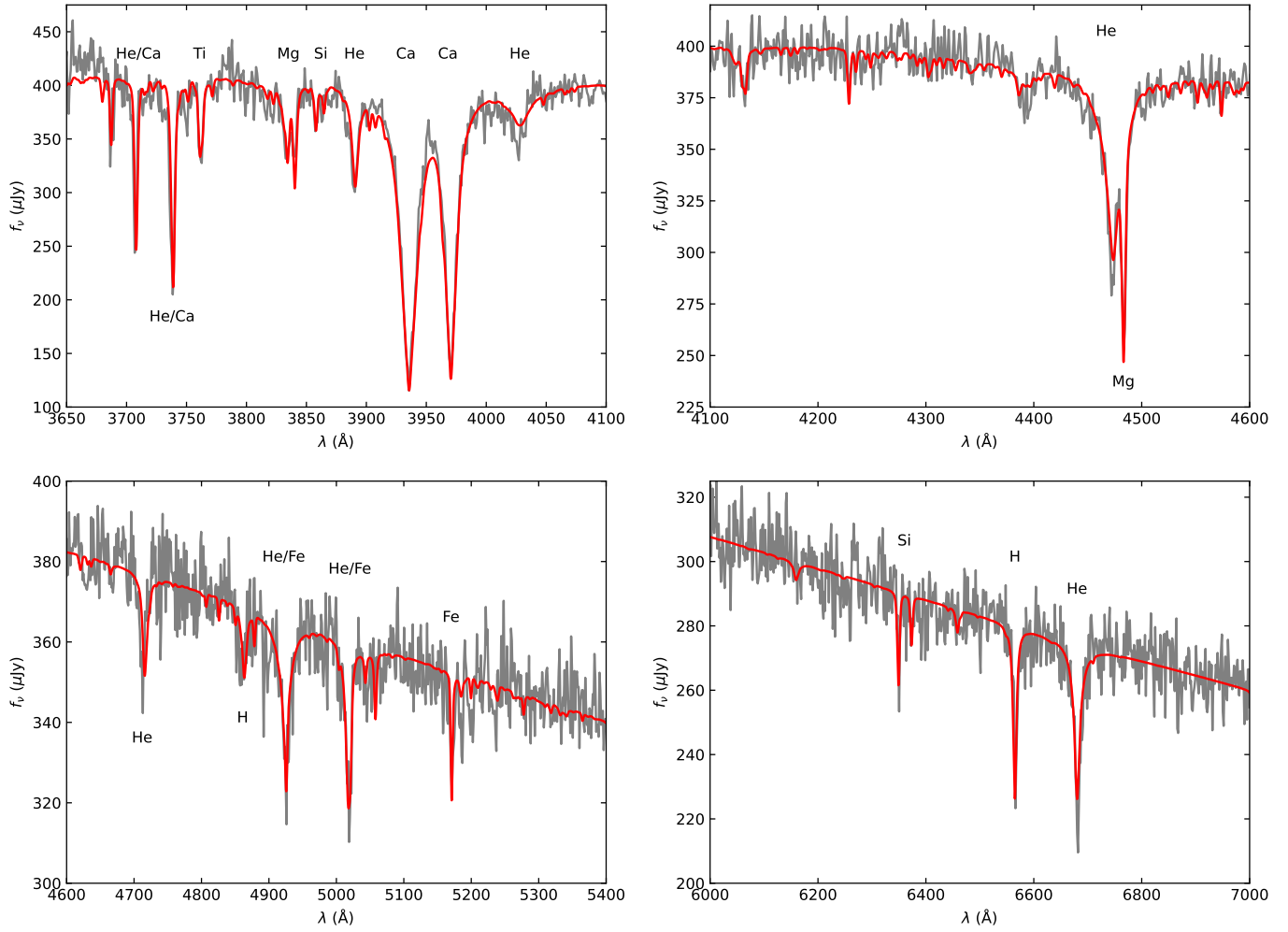


Fig. A.1: Four regions of the SDSS spectrum showing the best fitting atmospheric model to the data. Key lines have been labeled with their associated element.

Appendix B: Linelist for Element Abundance Measurements in HD69962

Element	Wavelength (nm)	$\log(gf)$	EP (eV)
Ca 1	610.2723	-0.85	1.879
Ca 1	612.2217	-0.38	1.886
Ca 1	643.9075	0.39	2.526
Ca 1	644.9808	-0.502	2.521
Ca 1	647.1662	-0.686	2.526
Cr 1	527.5747	-0.023	2.889
Cr 1	529.6691	-1.36	0.983
Cr 1	534.8314	-1.21	1.004
Mg 1	552.8405	-0.498	4.346
Na 1	568.8205	-0.404	2.104
Na 1	615.4225	-1.547	2.102
Na 1	616.0747	-1.246	2.104
Ni 1	504.2186	-0.58	3.658
Ni 1	509.9930	-0.10	3.679
Ni 1	542.4645	-2.77	1.951
Ni 1	546.2493	-0.818	3.847
Ni 1	561.4773	-0.573	4.154
Ni 1	564.1881	-1.046	4.105
Ni 1	580.5217	-0.579	4.167
Ni 1	585.7752	-0.402	4.167
Ni 1	600.7310	-3.40	1.676
Si 1	570.1104	-1.953	4.930
Si 1	570.8400	-1.370	4.954
Si 1	577.2146	-1.653	5.082
Si 1	612.5021	-1.464	5.614
Si 2	634.7109	0.169	8.121
Ti 2	501.3686	-2.14	1.582
Ti 2	506.9090	-1.62	3.124
Ti 2	507.2286	-1.02	3.124
Ti 2	518.8687	-1.05	1.582
Ti 2	522.6538	-1.26	1.566
Ti 2	541.8768	-2.13	1.582

Table B.1: Elemental line data including ionization state, wavelength, $\log(gf)$ values, and excitation potential (EP).